

**FURTHER INVESTIGATION OF THE TIME DELAY,
MAGNIFICATION RATIOS, AND VARIABILITY IN THE
GRAVITATIONAL LENS 0218+357**

A. S. Cohen, J. N. Hewitt

Department of Physics and Center for Space Research
Room 37-607, Massachusetts Institute of Technology, Cambridge, MA 02139
aaron@space.mit.edu, jhewitt@mit.edu

C. B. Moore

Harvard-Smithsonian Center for Astrophysics, 60 Garden Street
Cambridge, MA 02139
cmoore@cfa.harvard.edu

D. B. Haarsma

Department of Physics and Astronomy, Calvin College
Grand Rapids, MI 49546
dhaarsma@calvin.edu

and

Received _____; accepted _____

ABSTRACT

High precision VLA flux density measurements for the lensed images of 0218+357 yield a time delay of $10.1_{-1.6}^{+1.5}$ days (95% confidence). This is consistent with independent measurements carried out at the same epoch (Biggs et al. 1999), lending confidence in the robustness of the time delay measurement. However, since both measurements make use of the same features in the light curves, it is possible that the effects of unmodelled processes, such as scintillation or microlensing, are biasing both time delay measurements in the same way. Our time delay estimates result in a confidence intervals that are somewhat larger than those of Biggs et al., probably because we adopt a more general model of the source variability, allowing for constant and variable components. When considered in relation to the lens mass model of Biggs et al., our best-fit time delay implies a Hubble constant of $H_o = 71_{-23}^{+17}$ km s⁻¹ Mpc⁻¹ for $\Omega_o = 1$ and $\lambda_o = 0$ (95% confidence; filled beam). This confidence interval for H_o does not reflect systematic error, which may be substantial, due to uncertainty in the position of the lens galaxy. We also measure the flux ratio of the *variable* components of 0218+357, a measurement of a small region that should more closely represent the true lens magnification ratio. We find ratios of $3.2_{-0.4}^{+0.3}$ (95% confidence; 8 GHz) and $4.3_{-0.8}^{+0.5}$ (15 GHz). Unlike the reported flux ratios on scales of 0.1'', these ratios are not strongly significantly different. We investigate the significance of apparent differences in the variability properties of the two images of the background active galactic nucleus. We conclude that the differences are not significant, and that time series much longer than our 100-day time series will be required to investigate propagation effects in this way.

Subject headings: gravitational lenses, distance scale, BL Lacertae objects: individual (0218+357)

1. Introduction

Gravitational lenses provide unique opportunities to make cosmological measurements and to study distant sources and lensing galaxies. One such measurement is that of cosmological distance, without the assumptions inherent in intermediate distance indicators (Refsdal 1964; Refsdal 1966). The difference in the light travel time of the paths to the images is proportional to the angular diameter distance to the lens (if the mass scale in the lens can be determined independently) or to an “effective” distance, a combination of the angular diameter distances between the lens, observer, and source (Narayan 1991). The difference in the light travel time can be found from the time delay between flux variations in each lensed image. A mass model predicts the relationship between time delay and angular diameter distance. Thus, a time delay and a mass model can be used to determine independently the angular diameter distance to the lens. Another prediction of a gravitational lens model is the magnification ratio. This quantity can be used as a model constraint or as a means to investigate source structure on very small scales (see, for example, Conner, Lehár, & Burke 1992). Finally, studies of the variability of lensed images, particularly any differences in the variability properties, present a new tool for investigating propagation effects.

Gravitational lens monitoring observations were first carried out for the gravitational lens 0957+561, with time delays reported by Florentin-Nielsen (1984), Vanderriest et al. (1989), Lehár et al. (1992), Press, Rybicki, and Hewitt (1992a&b) and Oscoz et al. 1997, among others. (For a comprehensive review of time delay measurements in 0957+561 see Haarsma et al. 1997.) The results were conflicting and somewhat controversial, and the discrepancies have only recently been resolved (Kundić et al. 1997, Haarsma et al. 1999). Though these measurements, particularly those of Kundić et al., determine the delay with high precision, uncertainties in the lens model at present limit the accuracy of a distance determination in this system (Falco, Gorenstein & Shapiro 1991; Grogin & Narayan 1996a&b; Bernstein et al. 1997; Barkana et al. 1999; Bernstein & Fischer 1999). Recently time delays have been reported in other lens systems, including PG 1115+080 (Schechter et al. 1997), PKS 1830-211 (Lovell et al. 1998), HE 1104-1805 (Wisotzki et al. 1998), B1608+656 (Fassnacht et al. 2000), and B1600+434 (Koopmans et al. 2000). For most of these lenses as well, the modeling currently limits the determination of angular diameter distance. In order to refine significantly gravitational lens investigations of cosmography, it will probably be necessary to consider measurements of many lens systems as well as to improve individual lens models. With this goal in mind a number of lens monitoring

programs are under way.

The radio source 0218+357 was first proposed as a gravitational lens by Patnaik et al. (1993) and O’Dea et al. (1992). It consists of two images of a background BL Lac object, including a radio Einstein ring, and an extended jet and lobe emission that are not multiply imaged (see Figures 1 and 2). The radio ring has an unusually small diameter, only $0.35''$. The small ring, the detection of absorption lines attributed to neutral hydrogen (Carilli, Rupen & Yanny 1993) and various molecules (Wiklind & Combes 1995), the large rotation measure observed in linear polarization, and the lens optical colors and redshift (Keeton, Kochanek, & Falco 1998) suggest that the lensing object is a gas-rich spiral galaxy. The images of the radio core reveal a flat-spectrum component that has been imaged on VLBI scales (Patnaik, Porcas & Browne 1995, Patnaik & Porcas 1999). The lens redshift, based on optical (Browne et al. 1993) and radio absorption lines, is 0.685; the likely source redshift is 0.96 (Lawrence 1996).

VLA monitoring observations of 0218+357 have been carried out by Biggs et al. (1999), and they report a time delay of 10.5 ± 0.4 days (95% confidence). They also report significantly different flux ratios of 3.57 ± 0.01 and 3.73 ± 0.01 (68% confidence) at 8 GHz and 15 GHz, respectively. These results are based on data spanning approximately 100 days. The experience of 0957+561 has taught us that parameter fitting on a relatively small dataset may fail to be robust, with different analysis techniques yielding conflicting results. Delays based on a single feature may be unreliable due to the effects of unmodeled processes, such as scintillation or gravitational microlensing, which may bias the results. Therefore, repeated measurements and different analysis techniques should be brought to bear on the gravitational lens monitoring experiments. The analysis of Biggs et al. included features found in the polarization light curves as well as the flux density light curves, which in effect represent repeated measurements of the delay. We report in this paper an investigation of independent VLA measurements of the flux density of 0218+357, in which we used data reduction and parameter fitting techniques that differed from those of Biggs et al. We also adopt a more general model of the source variability, including the possibility of constant and variable components with different magnification ratios. A comparison of the results addresses the issue of the robustness of the parameter estimates. We caution, however, that since our monitoring observations occurred at the same epoch as those of Biggs et al., unmodeled scintillation or microlensing may be biasing both measurements.

2. Observations and Data Analysis

We present a set of 60 observations carried out with the National Radio Astronomy Observatory (NRAO) Very Large Array (VLA) telescope.¹ Continuum observations (with 100 MHz bandwidth) were carried out between 1996 October 9 and 1997 January 14 in the A configuration at both 8 GHz and 15 GHz. The flux density scale was set by observations of 3C48, and observations of 0205+322 were used to compute complex antenna gains. Both senses of circular polarization were recorded. The time on source per observation varied, but the averages were 5 and 10 minutes for the 8 GHz and 15 GHz observations, respectively. The theoretical thermal map noise for the average observation time is $64 \mu\text{Jy}/\text{beam}$ at 8 GHz, and $170 \mu\text{Jy}/\text{beam}$ at 15 GHz. However, as we discuss below, the error in measuring the flux densities of the two point sources in the map is dominated by other effects.

The data were calibrated using the NRAO’s Astronomical Image Processing Software (AIPS) software. At each frequency a reference model based on a CLEAN deconvolution (Högbom 1974, Clark 1980) was adopted. For the reference models, data taken on 1996 November 9 (8 GHz) and 1996 November 8 (15 GHz) were used. Phase corrections with respect to this model were computed, and the AIPS task IMAGR was used to create naturally weighted maps and to deconvolve (again using the CLEAN algorithm) the maps. The AIPS task CALIB was used to self-calibrate the phases with respect to the CLEAN components of each map, restoring the flux densities to the values appropriate to the data, minimizing the bias of the reference model. The process of CLEANing and self-calibration was carried out until the flux densities of the A and B compact components converged, usually requiring three iterations. The typical synthesized beam full width at half maximum was $0.24''$ at 8 GHz and $0.14''$ at 15 GHz, barely resolving the $0.334''$ separation of A and B at 8 GHz. Each UV data set was rotated, shifted and scaled so that in the resulting map each of the two point sources fell exactly at the center of an image pixel. We estimated the flux density of A and B as the value of the flux density at these two image pixels. Typical maps are displayed in Figures 1 and 2.

In contrast to the method used by Biggs et al., we did not attempt to fit the UV data to a model, because the precise structure of the ring and jet is uncertain and may be too complicated for approximation by a simple model. Error in our technique is introduced by

¹The National Radio Astronomy Observatory is operated by Associated Universities, Inc., under cooperative agreement with the National Science Foundation.

the fact that the size and shape of the synthesized beam varies slightly from map to map. One approach to remove this source of error might be to convolve all clean components with a standard clean beam before restoring them to the residual map. However, the different UV samplings in fact measure different parts of the unknown structure, so with this approach unknown levels of residual systematic error are likely to remain. As discussed below we chose instead to use our measurements of the source structure and the UV coverage of each observation to compute the error and correct the flux density measurements. This technique has been shown to be extremely effective in tests with the non-varying source MG0414+0534, giving flux density uncertainties dominated by flux density calibration errors and as small as 1% (Moore and Hewitt, submitted). In 0218+357 the presence of substantial extended emission complicates the analysis, but the correction of bias due to UV sampling is nonetheless critical. In any case, our flux density estimation technique differs substantially from that of Biggs et al., and comparison of our results will provide a check for systematic error.

One source of error in the flux density estimates of each point source is confusion from the diffuse emission from the ring and confusion from the other point source. The flux of the ring is presumed constant, and the contamination from the other point source is reduced by at least a factor of 100 by its separation and the properties of the synthesized beam. The confusion from the diffuse emission changes as the UV-coverage changes. We correct for this by creating a synthetic image based on a static model of the source. The static model consists of a set of CLEAN components, obtained from one high quality image, which are Fourier transformed onto the points in the UV plane that each individual observation sampled. This synthetic dataset for each observation was reduced using exactly the same methods as for the real data, and any resulting variations in the flux densities are due only to the variations in the UV coverage. These variations represent multiplicative correction factors which we applied to the light curves. This procedure produced light curves in which the flux densities represent that of each point component plus some level of outside contamination which should be essentially constant. A constant contribution to the flux density, which includes the outside contamination as well as the constant part of the point source flux density, is a parameter for which we fit when we perform our final analysis in Section 4.

A second source of error is in the flux calibration procedure. Because 3C48 is heavily resolved at both frequencies, we constructed a model for the source by combining all our 3C48 data. We determined our flux density scale over a limited UV range with respect

to this model, allowing a wider range of UV spacings to be used in the flux calibration and increasing its reliability. We also applied antenna gain corrections as a function of elevation (R. Perley, private communication). Despite our precautions, there is evidently still an overall flux density scale error which changes A and B by the same factor in each observation. Treating the phase calibrator, 0205+322, as a flux calibrator only increased the scatter in the light curves, indicating 0205+322 is variable. We therefore adopt the flux density calibration based on 3C48, accepting a certain amount of correlated error, which we identify and treat as such in our analysis. We believe that the flux density scale is the dominant source of error in our light curves.

3. Results: The Light Curves

In deriving our final light curves and their errors, we first eliminated some of the original 60 observations that were unreliable because of bad weather. We removed observations with reports of cumulus cloud cover of more than 50%, high wind, or precipitation. That left 51 data points over a ~ 100 day period for both frequencies. To estimate our measurement errors, we used the smoothness of the light curves and took as our error estimate the average fractional difference between points on our light curve that are separated by less than two days. This assumes that within any two-day time period, the variations are dominated by measurement errors and not actual source variability. To the extent that this is not true, we can consider our result to be an upper limit on the measurement errors. For the 8 GHz light curves, the errors are 0.49% and 0.62% for A and B, respectively. For the 15 GHz light curves, the errors are 1.4% and 1.2% for A and B, respectively. The relative levels of correlated and uncorrelated error were determined by assuming they add in quadrature and by comparing the A light curves with the flux ratios as a function of time (see Figure 3). The error in the A light curve alone is the total measurement error, while that in the A/B light curve represents only the uncorrelated error, since the correlated errors divide out. We find 0.33% and 0.99% for the correlated errors at 8 and 15 GHz respectively.

Our final light curves are listed in Table 1 and plotted in Figure 4. At both frequencies, there is a slow rise followed by a sharp decline in the flux density of each component, in agreement with the features seen by Biggs et al. The sharp decline clearly occurs first in the A component, then in the B component. The fractional variability is greater in the 15 GHz light curves, but the signal-to-noise ratio is greater in the 8 GHz light curves. The A/B flux density ratios are apparently not the same at both frequencies, in conflict with

the achromatic nature of gravitational lensing. This discrepancy is probably primarily due to confusion from the ring and the different resolution at the two frequencies. It is also possible, and in fact likely, that the A and B images are made up of constant and varying components with different spectral indices and magnification ratios (see Patnaik & Porcas 1999, Press & Rybicki 1998). As discussed below, we take this into account by assuming a variability model that consists of these two components, constant and varying.

4. Results: Time Delays and Flux Ratios

4.1. Statistical Methods

One can easily estimate the time delay between the light curves of components A and B by eye, but it is preferable to have an objective method that gives reproducible results and a quantitative estimate of the errors. Two methods are used in this paper. The first is the maximum likelihood method of Press, Rybicki & Hewitt (1992a,b; henceforth PRH) and Rybicki & Kleyana (1994), modified to account for the fact that some of flux we are measuring could be constant and unrelated to the varying part (Press & Rybicki 1998). The second method is the “minimum dispersion method” of Pelt et al. (1994, 1996).

The first step in the PRH method is to determine the correlation properties of the light curve as a function of time lag between measurements, where we expect a greater correlation between measurements that have smaller separations in time. We fit a first-order structure function to the data, modeling it as a power law:

$$V(\tau) \equiv \frac{1}{2} \langle [f(t) - f(t - \tau)]^2 \rangle = K\tau^\alpha \quad (1)$$

where $f(t)$ a measurement at time t , τ is the time lag, and K and α are parameters that we fit (Simonetti, Cordes & Heeschen 1985; Edelson & Krolik 1988). Since we do not know the flux ratio, we take $f(t)$ to be the natural logarithm of the flux density measured at time t referred to 1 mJy, removing the dependence of our analysis on the unknown flux ratio.

As will be discussed in more detail in Section 6, we do not have enough data to measure the intrinsic structure function ourselves with a high degree of accuracy. Therefore, we have to refer to other data and theory about extragalactic variable sources in general to make reasonable assumptions. In particular, long-term monitoring the flux density of many quasars and BL Lac objects (Hughes, Aller & Aller 1992) show that for quasars, the structure function value of α is 1.04 ± 0.18 for light curves which are not dominated by a

single feature (which tends to give an upward bias on the measurement of α). For BL Lac objects, $\alpha = 0.94 \pm 0.37$. There are also theoretical arguments that are consistent with this; the value of α is exactly unity for such natural random processes as shot noise and random walk. It is reasonable, therefore, to assume that $\alpha = 1$ in the intrinsic structure function, and we do so in our analysis.

The next step in the PRH method is to test whether a single light curve, constructed by combining the A and B light curves according to trial parameters, has the same statistical properties as the individual light curves. The combining of the A and B light curves is done nominally according to four parameters. The first is the time delay T , which results in the points from the B light curve being shifted back in time by the amount T . The second parameter is the magnification ratio; when combining the light curves the B points must be multiplied by a magnification ratio, R . Since we allow for the fact that each component contains a constant component as well as a varying component, we specify that R be the flux ratio (A/B) of the variable components only. That leaves the constant parts of A and B (C_A and C_B) as our third and fourth parameters. However, as shown by Press and Rybicki (1998), we cannot solve for both C_A and C_B . The parameter for which we can solve is $C_o = RC_B - C_A$, which essentially tells us the difference in the constant flux densities of A and B. The resulting three *independent* parameters are fit so as to best match the statistical properties of the recombined light curve to that of the individual light curves as described by the structure function.

As discussed by PRH and Rybicki and Kleyna (1994), the degree of “matching” is quantified by their so-called “Q-statistic”

$$Q = \mathbf{y}^T \mathbf{B}^{-1} \mathbf{y} - \ln \det(\mathbf{B}^{-1}) \quad (2)$$

where \mathbf{y} is the vector of flux density values for the recombined light curve and \mathbf{B} is the total covariance matrix as defined by PRH. The elements of the covariance matrix describe the statistical properties of the light curve. If we separate the measurement errors, $e(t)$ from the true flux density, $s(t)$, then the measured flux density is

$$f(t) = s(t) + e(t), \quad (3)$$

which implies that

$$B_{ij} = \langle s^2(t) \rangle - V(\tau) + \langle e(t_i)e(t_j) \rangle. \quad (4)$$

The first term on the right-hand side is simply the average square of the flux density values and is the same for all B_{ij} . The second term is the structure function that we have estimated

empirically. The last term is zero, except for two cases. The first case is when $i = j$ and $\langle e(t_i)e(t_j) \rangle = \langle e^2(t) \rangle$, the average square of the measurement errors. The other case occurs when $i \neq j$ but (because of the shift by the time delay) the two flux density measurements come from the same observations and so the errors are not uncorrelated. In this way we account for the correlated flux density scale errors. Combining the light curves for trial values of T , R , and C_o , we find the best-fit values of these parameters by minimizing the Q-statistic.

The Pelt et al. minimum dispersion method is similar to the PRH method in that it also attempts to find recombination parameters that minimize a statistical quantity associated with the combined light curve. The quantity in this case is the dispersion, which is defined as the average square of the difference in flux density values of nearby points in the light curve. “Nearby” is defined as points that are spaced apart in time by less than the decorrelation length, δ . The contribution of any such pair of points is then weighted by the factor $(1 - \tau/\delta)$ where τ is the time between the two points (Pelt et al. 1996). Since we give all the points in the light curves equal weight, our dispersion statistic is:

$$D = \frac{\sum_{i,j} S_{i,j} (f(t_i) - f(t_j))^2 (1 - \frac{\tau}{\delta})}{\sum_{i,j} S_{i,j} (1 - \frac{\tau}{\delta})} \quad (5)$$

where

$$\tau = |t_i - t_j| \quad \text{and} \quad S_{i,j} \begin{cases} = 1 & \text{if } \tau < \delta \\ = 0 & \text{if } \tau \geq \delta \end{cases} \quad (6)$$

As in the PRH method, we fit T , R , and C_o so as to minimize the dispersion in the combined light curve. It is unclear, however, what value to use for δ . Therefore, we tried a range of values of δ and found best-fit values of the parameters as a function of δ .

4.2. Results of the PRH Method

Empirical estimates of the A and B structure functions for the two frequencies were formed by binning the 1275 pairs from the 51 data points (see Figure 5). The finite time series do not provide fair samples of the larger time lags, so only the first section of the structure functions (from 0 to about 50 days) were used in the fit to the power law model. Since we assume $\alpha = 1$, we fit only for K . For the purpose of the time delay analysis, structure functions were fit to both the A and B light curves, and at each frequency the results were averaged ($\langle K \rangle = \sqrt{K_A K_B}$), giving $\langle K \rangle = 1.2 \times 10^{-5}$ at 8 GHz and

$\langle K \rangle = 3.1 \times 10^{-5}$ at 15 GHz. Finally the light curve recombination parameters were fit as described above. The results were $T = 9.60$ days, $R = 3.15$, and $C_o = 113$ mJy for 8 GHz; and $T = 11.3$ days, $R = 4.25$, and $C_o = 176$ mJy for 15 GHz.

4.3. Results of the Minimum Dispersion Method

The results of the minimum dispersion method are shown in Figure 6, plotted as a function of the assumed decorrelation length δ . The results vary by $\pm 10\%$ as a function of δ , even without any consideration of the errors in the parameters. The values of T are generally centered around the values we found with the PRH method. However, since we have no knowledge of the actual value of δ for either light curve, we conclude that no definitive determination of the parameters could be made with the dispersion method. Although successful in determining the time delay in 0957+571 (Pelt et al. 1996), the method is inconclusive here, probably because in this case we have a much shorter monitoring period.

5. Error Analysis

To estimate the accuracy of our parameter fitting procedure, we repeated the PRH analysis with two sets of simulated data. The first set assumes that the underlying process producing the light is gaussian; the second makes no such assumption and instead derives the simulated data from the real data.

5.1. Gaussian Monte Carlo Simulations

As described by PRH, we created simulated light curves with the same sampling in time as the true light curves, assuming a gaussian process with the structure function and errors that we derived from the measured light curves. The measurement errors consisted of both correlated and uncorrelated parts, as described in Section 3.

5.1.1. *Errors Due to an Incorrect Structure Function*

Our first application of the Monte Carlo simulations was to investigate the effect of an incorrect structure function on our estimate of the time delay, T . For each light curve, simulations were performed with the assigned time delay varying randomly and uniformly between 0 and 20 days. The differences between the actual time delays and the fitted time delays were computed, and standard deviations of the set of differences were calculated. It is important to realize that for these calculations *two* structure functions are involved. The first is used to create the simulated data, and we call this the “true” structure function. The second is the one we fit to the simulated data in the process of estimating the time delay; we call this the “assumed” structure function. Varying both the true and assumed structure functions in our simulations allows us to test the effects of an incorrect assumed structure function on our time delay estimation, as a function of the true structure function.

Of the two free parameters in a structure function, K and α , the value of α was chosen and the value of K was fitted, reproducing our analysis procedure. For the “true” structure functions a “true” α was chosen and the “true” K was fit to the real (measured with the VLA) light curves. For the “assumed” structure functions an “assumed” α was chosen and the “assumed” K was fit to the simulated light curves. Then the effectiveness of the PRH method was tested for values of “true” α and “assumed” α that ranged in five steps from 0.50 to 1.50. For each case, we performed 1,000 Monte Carlo simulations. The first result of this test showed that the average deviation between the actual time delay and the PRH-deduced time delay was less than .02 days. This was the case regardless of how the “true” and “assumed” values of α were varied. Therefore, it seems unlikely that an incorrect “assumed” structure function could have produced a significant bias in the time delay measurements. However, the error estimates for each measurement did change somewhat as the structure functions were varied. Table 2 shows how the error estimates change as function of “true” α and “assumed” α . The “true” α has much more of an effect on the error estimates than the “assumed” α . This indicates that the magnitude of the error estimates depends mostly on the intrinsic structure function of the BL Lac object and very little on the accuracy of the fitted structure function. Thus, the reliability of our error estimates appear to be limited by our knowledge of the intrinsic structure function. In all further simulations we assume $\alpha = 1$.

5.1.2. Confidence Intervals

After settling on a reasonable structure function, we concentrate on our ability to determine confidence intervals for the three parameters T , R , and C_o . We expect T and possibly R to be the same for both frequencies, but the C_o parameter is likely to be different at the two frequencies. We again constructed Monte Carlo light curves, but now varying the assigned values of all three parameters: T was varied between 8 and 12 days; R was varied between 2 and 5; and C_o was varied between 0 and 200 mJy. For the light curves, the fitted values were compared to the true values, and 95% confidence intervals were derived and adopted as the errors on the parameter estimates. The distributions are shown in Figure 7. The parameters T and R for the two frequencies were averaged, weighted according to their errors. The results are presented in Table 3.

5.2. Jackknife Samples

The confidence intervals derived in the previous section are based on the assumption that the underlying process producing the quasar light curves is a gaussian process and on the model we assumed for the errors. This is a weakness of our gaussian Monte Carlo technique, and we seek to explore methods that derive the statistics of the process from the data themselves. One such method is the jackknife (Tukey 1958; see also Efron & Tibshirani 1993), in which “jackknife samples” are formed by successively deleting one point from the data set. We applied this technique to our light curves at both frequencies, estimating the T , R , and C_o parameters for each jackknife sample and forming distributions of the fitted values, shown in Figure 8.

We compute errors on the parameters by forming the 95% confidence intervals from the data of Figure 8, which have been rescaled by the necessary “expansion factor” $(N - 1)/\sqrt{N}$ (see Efron & Tibshirani 1993). Values from the different frequencies for T and R are combined as described above, and the results are presented in Table 4. We caution that since the light curve data points are not independent, the jackknife simulations are likely to underestimate the true errors.

5.3. Evaluation of Errors

If we compare the error distributions generated by the two different simulation techniques (Figures 7 and 8), a couple of interesting differences emerge. First, the jackknife distribution for the time delays is very different from the corresponding Monte Carlo distribution, and it clearly is not gaussian. This is an indication that the Monte Carlo simulations are failing to capture the properties of the data in a way that causes estimation of the time delay distribution to be unreliable. Therefore, we adopt the jackknife errors as our errors on T . Second, the jackknife distribution for R and C_o are not as broad as the corresponding Monte Carlo distribution, but do appear gaussian, indicating that the R and C_o estimation process is better behaved than the T estimation process. However, since there is reason to suspect the jackknife procedure may underestimate the true errors, we adopt the Monte Carlo errors as our errors on R and C_o . The differences in the distributions in Figures 7 and 8 illustrate the difficulty of reliable error estimation in these light curves, a topic that deserves further study. With the confidence intervals determined, we now see that the best-fit values of T for the two observing frequencies are not significantly different, and we form a weighted average. The best-fit values of R are only marginally significantly different, so we also compute its average. Our final results, with 95% confidence intervals, are: $T = 10.1_{-1.6}^{+1.5}$ days, $R = 3.2_{-0.4}^{+0.3}$ (8 GHz), $R = 4.3_{-0.8}^{+0.5}$ (15 GHz), $R = 3.4_{-0.4}^{+0.2}$ (averaged), $C_o = 110_{-110}^{+80}$ (8 GHz), and $C_o = 180_{-140}^{+100}$ (15 GHz). We reiterate that the jackknife errors used for the time delay are likely to be an underestimate. The light curves superimposed according to the best-fit parameters are shown in Figure 9.

6. Are the Structure Functions Significantly Different?

The A and B structure functions appear different (Figure 5), with component B more strongly auto-correlated at small lags than component A. Since radiation from the two components travels along different paths to reach the observer, such a comparison may reveal differences in propagation characteristics, such as scintillation or gravitational microlensing. In this section we investigate the significance of the apparent differences in the structure functions.

The points plotted in Figure 5 represent bin averages. If the (assumed white) light curve measurement noise is σ_m and there are N points in a bin, then the standard error of

the structure function estimate in that bin is approximately

$$\sigma_V = \frac{2\sigma_m}{\sqrt{N}}\sqrt{V(\tau)} \quad (7)$$

(Simonetti, Cordes & Heeschen 1985, corrected for our choice of scaling of the structure function), assuming a long time series. However, our time series is truncated after only 100 days, so we cannot necessarily assume the lags are fairly sampled. Therefore, we have addressed this empirically by further Monte Carlo simulation.

We again remove the dependence of $V(\tau)$ on the assumed flux ratio by working in natural logarithmic units, referenced to 1 mJy. A power law structure function was fit to the data, but now allowing the parameter α to vary and fitting separately for components A and B at the two frequencies. The four resulting structure function models were used to generate four sets of gaussian Monte Carlo simulations, of 1000 realizations each, and structure functions were computed for all the simulated data sets. From these the mean and the 68% confidence interval were computed for each value of τ . The results are the error bars shown in Figure 5. Although our error estimates are to some extent model dependent, the differences in the structure functions are not significant. Much longer time series would be necessary to explore propagation effects in this way.

7. Comparison with Previous Measurements

Our time delay value of $10.1_{-1.6}^{+1.5}$ days (95% confidence) is consistent with the value found by Biggs et al. and lends confidence to the robustness of the time delay measurements. Our results are derived from an independent set of data, very different data reduction techniques, very different parameter fitting techniques, and more general models for both the measurement errors and the variability of the background object. The light curves produced by the two analyses are in excellent agreement, showing the same major feature. However, this is also a weakness of the comparison. It is possible that this feature is affected by microlensing or scintillation, and both analyses of the data would be biased in the same way if this is the case (see Haarsma et al. 1999 for a discussion of such bias in the 0957+561 lens system). While there is no evidence for microlensing or scintillation in the light curves of 0218+357, only measurements at another epoch can reduce this uncertainty.

Our error analysis results in confidence intervals for the time delay that are somewhat larger than those of Biggs et al. The errors on our flux density measurements are smaller than those of Biggs et al. at 8 GHz, larger at 15 GHz, but in both cases not much different.

Therefore, it appears the source of the difference in confidence intervals is in the time delay fitting procedures rather than in the light curve errors. Since we parameterize our variability model differently, with three parameters associated with each light curve rather than two, it is not surprising that our confidence intervals are larger. In fact, we caution that in general an oversimplification of the model may result in deceptively small confidence intervals.

In the derivation of magnification ratios, Biggs et al. parameterized their model in terms of the ratios of the total flux densities. We separate the variable and constant parts of the flux densities, fitting for the magnification ratio associated with the variable part. Biggs et al. find very different flux ratios at 8 and 15 GHz; the values differ by more than ten standard deviations. As discussed above, such differences may be caused by different source structure at the different frequencies, combined with lens magnification gradients and the nonzero resolution of the observations. Our fitting procedure represents an attempt to derive the true magnification ratio of the *variable part* of the source that presumably is small in angular size. The importance of this quantity is that the observational effects that cause flux ratio differences at different frequencies should be greatly reduced, and we are measuring the true lens magnification that is important in constraining lens models.

The fitting of our more general model shows that for the existing data there is a degeneracy between the C_o and the R parameters, so that without independent information on C_o the value of R is rather poorly determined. Therefore, we find larger confidence intervals for the values of R at the two frequencies, with the confidence intervals including the values found by Biggs et al. The experience of 0957+571 shows that a longer series of data that includes both variable and quiescent behavior of the quasar should determine with more precision the magnification ratio of the variable part of the source.

The implied value of the Hubble constant for a particular lens model scales with the measurement of the time delay. Therefore, applying our time delay value to the model of Biggs et al. yields $H_o = 71_{-23}^{+17} \text{ km s}^{-1} \text{ Mpc}^{-1}$ at 95% confidence level, necessarily consistent with their result. This model assumes a flat universe in which $\Omega_o = 1$ and $\lambda_o = 0$ (filled beam). Lehár et al. (2000) have also attempted to model the 0218+357 lens, and they conclude that the uncertainties are larger than those found by Biggs et al. We await the results of planned VLBA measurements of the radio ring before tackling the problem of modeling the lens. In any case, the above value of H_o is consistent with other recent measurements. For example, a value of $H_o = 71 \pm 6 \text{ km sec}^{-1} \text{ Mpc}^{-1}$ (67% confidence interval) was determined by the HST key project collaboration (Mould et al. 1999), and

a value of $H_o = 81 \pm 4$ (67% confidence interval) was derived from a recalibration of the Cepheid distance scale (Maoz et al. 1999) based on a geometric distance to NGC 4258 (Herrnstein et al. 1999). At this time, the time delay and mass model uncertainties are still large enough to preclude any rigorous attempts to test cosmological models with the 0218+357 lens system.

8. Conclusions

VLA flux density measurements for the lensed images of 0218+357 have been carried out with errors of 1% or less, even with only five to ten minutes of dwell time on source. This precision is important in time delay measurements because the variability of the background object is often limited. We find a time delay of $10.1_{-1.6}^{+1.5}$ days (95% confidence). We find magnification ratios associated with the *variable* part of the light curves of $3.2_{-0.4}^{+0.3}$ (8 GHz), $4.3_{-0.8}^{+0.5}$ (15 GHz), and $3.4_{-0.4}^{+0.2}$ (averaged). We find best-fit values (which are rather poorly determined) of the difference in the constant part of the light curves of 110_{-110}^{+80} mJy (8 GHz) and 180_{-140}^{+100} mJy (15 GHz). Our results, when compared to those of Biggs et al., indicate that the time delay measurement is very robust in this system. The magnification is relatively poorly determined because it is difficult to separate the variable and constant part of the light curves; however, this quantity is the one properly associated with the true magnification of the lens and is needed for lens modeling. Our values for the magnifications at the two frequencies are different at about the 3σ level. However, given the uncertainties involved in determining confidence intervals, we do not feel this is strong enough evidence to claim frequency-dependent magnification ratios. Monte Carlo simulations of structure function estimation have shown that the structure functions are also poorly determined. Thus, examining any differences in the variability properties of lensed images, which would be interesting in the investigation of propagation effects, would require much longer time series than are available in this system at present. We have demonstrated numerically that this uncertainty in the structure functions does not significantly impact the time delay estimation, as expected from theoretical considerations (Press, Rybicki and Hewitt 1992a,b). For the lens model of Biggs et al., the measured time delay implies a Hubble constant of $H_o = 71_{-23}^{+17}$ km s⁻¹ Mpc⁻¹ for $\Omega_o = 1$ and $\lambda_o = 0$ (95% confidence, filled beam). However, this confidence interval does not reflect systematic error, which may be substantial, due to the uncertainty in the position of the lens galaxy.

Gravitational lenses provide a way to determine the value of H_o directly, without any

dependence on intermediate distance indicators. This requires more data and modeling than currently exist. Of particular value would be to combine angular diameter distance measurements for many different lensed systems. As more lenses are monitored for longer periods, the time delays inevitably will become far more accurate and numerous. This leaves the lens models as the limiting factor in individual angular diameter distance measurements. Each lens is unique in this respect, but in general models can be improved by extensive observing at various frequencies and resolutions. Such measurements improve the flux density and positional information about the multiply imaged source components and the lensing mass, and provide a greater number of modeling constraints. In the lens system 0218+357, there is a full Einstein ring in addition to the doubly imaged radio core. This ring is difficult to observe in detail because it is small (about 350 mas in diameter) and very faint compared to the radio cores. However, an accurate map of the fine structure in the ring will add many more constraints to any existing models of this system and greatly improve their accuracy. This is probably the best way to improve the measurement of the angular diameter distance to this lens.

We gratefully acknowledge the assistance of the VLA staff in the preparation and execution of the extensive observations described in this paper. This work was supported in part by grant AST-9617028. A.S.C. acknowledges the support of an NSF Graduate Fellowship; D.B.H. acknowledges the support of a Cottrell College Science Award from Research Corporation. We thank the referee, A. Biggs, for extensive comments that led to improvements in the manuscript.

REFERENCES

- Barkana, R., Lehár, J., Falco, E. E., Grogin, N. A., Keeton, C. R., and Shapiro, I. I. 1999, *ApJ*, 520, 479.
- Bernstein, G., Fischer, P., Tyson, J. A. & Rhee, G. 1997, *ApJ*, 483, L79.
- Bernstein, G. M., and Fischer, P. 1999, *AJ*, 118, 14.
- Biggs, A. D., Browne, I. W. A., Helbig, P., Koopmans, L. V. E., Wilkinson, P. N., & Perley, R. A. 1999, *MNRAS*, 304, 349.
- Browne, I. W. A., Patnaik, A. R., Walsh, D., & Wilkinson, P. N. 1993, *MNRAS*, 263, L32.
- Carilli, C. L., Rupen, M. P., & Yanny, B. 1993, *ApJ*, 412, L59.
- Clark, B. G. 1980, *AA*, 89, 377.
- Conner, S. R., Lehár, J., & Burke, B. F. 1992, *ApJ*, 387, 61.
- Edelson, R. A., & Krolik, J. H. 1988, *ApJ*, 333, 646.
- Efron, B., & Tibshirani, R. J. 1993, *An Introduction to the Bootstrap* (New York:Chapman & Hall, Inc.), 141-150.
- Falco, E. E., Gorenstein, M. V., & Shapiro, I. I. 1991, *ApJ*, 372, 364.
- Fassnacht, C. et al. 2000, *ApJ*, in press.
- Florentin-Nielsen, R. 1984, *AA*, 138, L19.
- Grogin, N. A., & Narayan, R. 1996a, *ApJ*, 464, 92.
- Grogin, N. A., & Narayan, R. 1996b, *ApJ*, 473, 570.
- Haarsma, D. B., Hewitt, J. N., Lehár, J., & Burke, B. F. 1997, *ApJ*, 479, 102.
- Haarsma, D. B., Hewitt, J. N., Lehár, J., & Burke, B. F. 1999, *ApJ*, 510, 64.
- Herrnstein, J. R., Moran, J. M., Greenhill, L. J., Diamond, P. J., Inoue, M., Nakai, N., Miyoshi, M., Henkel, C. & Riess, A. 1999, *Nature*, 400, 539.
- Högbom, J. 1974, *ApJS*, 14, 417.

- Hughes, P. A., Aller, H. D., & Aller, M. F. 1992, *ApJ*, 399, 16.
- Keeton, C. R., Kochanek, C. S., & Falco, E. E. 1998, *ApJ*, 509, 561.
- Koopmans, L. V. E., de Bruyn, A. G., Xanthopoulos, E., & Fassnacht, C. D. 2000, *AA*, 356, 391.
- Kundić, T., Turner, E. L., Colley, W. N., Gott, J. R., III, Rhoads, J. E., Wang, Y., Bergeron, L. E., Gloria, K. A., Long, D. C., Malhotra, S., & Wambsganss, J. 1997, *ApJ*, 482, 75.
- Lawrence, C. R. 1996 in *Proc IAU Symp. 173, Astrophysical Applications of Gravitational Lensing* (eds. C. S. Kochanek & J. N. Hewitt), Kluwer, Dordrecht, 299.
- Lehár, J., Hewitt, J. N., Burke, B. F., & Roberts, D. H. 1992, *ApJ*, 387, 61.
- Lovell, J. E. J., Jauncey, D. L., Reynolds, J. E., Wieringa, M. H., King, E. A., Tzioumis, A. K., McCulloch, P. M., & Edwards, P. G. 1998, *ApJ*, 508, 51.
- Maoz, E., Newman, J. A., Ferrarese, L., Stetson, P. B., Zepf, S. E., Davis, M., Freedman, W. L. & Madore, B. F. 1999, *Nature*, 401, 351.
- Mould, J. R., Huchra, J. P., Freedman, W. L., Kennicutt, R. C., Jr., Ferrarese, L., Ford, H. C., Gibson, B. K., Graham, J. A., Hughes, S., Illingworth, G. D., Kelson, D. D., Macri, L. M., Madore, B. F., Sakai, S., Sebo, K., Silbermann, N. A. & Stetson, P. B. 1999, preprint astro-ph/9909260.
- Narayan, R. 1991, *ApJ*, 378, 5.
- O’Dea, C. P., Baum, S. A., Stanghellini, C., Dey, A., van Breugel, W., Deustua, S., & Smith, E. P. 1992, *AJ*, 104, 1320.
- Oscos, A., Mediavilla, E., Goicoechea, L. J., Serra-Ricart, M., & Buitrago, J. 1997, *ApJ*, 479, L89.
- Patnaik, A. R., Browne, W. A., King, L. J., Muxlow, T. W. B., Walsh, D., & Wilkinson, P. N. 1993, *MNRAS*, 261, 435.
- Patnaik, A. R., & Porcas, R. W. 1999, in *ASP Conf. Series Vol. 156, Highly Redshifted Radio Lines* (eds. C. I. Carilli, S. J. E. Radford, K. M. Menten & G. I. Langston).
- Patnaik, A. R., Porcas, R., & Browne, I. W. A. 1995, *MNRAS*, 274, L5.

- Pelt, J., Hoff, W., Kayser, R., Refsdal, S., & Schramm, T. 1994, AA, 286, 599.
- Pelt, J., Kayser, R., Refsdal, S., & Schramm, T. 1996, AA, 305, 97.
- Press, W. H., Rybicki, G. B., & Hewitt, J. N. 1992a, ApJ, 385, 404.
- Press, W. H., Rybicki, G. B., & Hewitt, J. N. 1992b, ApJ, 385, 416.
- Press, W. H., & Rybicki, G. B. 1998, ApJ, 507, 108.
- Refsdal, S. 1964, MNRAS, 128, 307.
- Refsdal, S. 1966, MNRAS, 132, 101.
- Rybicki, G. B., & Kleyana, J. T., 1994, in Reverberation Mapping of the Broad-Line Region in Active Galactic Nuclei, ed. P. M. Gondhalekar, K. Horne, & M. Peterson (San Francisco: Astronomical Society of the Pacific), 85.
- Schechter, P. L., Bailyn, C. D., Barr, R., Barvainis, R., Becker, C. M., Bernstein, G. J., Blakeslee, J. P., Bus, S. J., Dressler, A., Falco, E. E., Fesen, R. A., Fischer, P., Gebhardt, K., Harmer, D., Hewitt, J. N., Hjorth, J., Hurt, T., Jaunsen, A. O., Mateo, M., Mehlert, D., Richstone, D. O., Sparke, L. S., Thorstensen, J. R., Tonry, J. L., Wegner, G., Willmarth, D. W., & Worthey, G. 1997, ApJ, 475, 85.
- Simonetti, J. H., Corrdes, J. M., & Heeschen, D. S. 1985, ApJ, 296, 46.
- Tukey, J. W. 1958, Ann. Math. Statist., 29, 614.
- Vanderriest, C., Schneider, J., Herpe, G., Chevreton, M., Moles, M., & Wlerick, G. 1989, AA, 215, 1.
- Wiklind, T., & Combes, F. 1995, AA, 299, 382.
- Wisotzki, L., Wucknitz, O., Lopez, S., & Sorensen, A. N. 1998, AA, 339, L73.

8 GHz Flux Densities			15 GHz Flux Densities		
Days since Julian Day 2450365	Flux Density of A (mJy)	Flux Density of B (mJy)	Days since Julian Day 2450365	Flux Density of A (mJy)	Flux Density of B (mJy)
3.81	846.7	301.0	1.75	776.0	217.3
4.67	847.5	301.8	3.81	797.7	230.0
5.83	836.4	298.6	4.67	793.4	227.6
6.83	835.5	300.3	5.83	799.9	230.1
7.77	832.8	296.6	6.83	776.8	227.0
9.79	838.2	301.2	7.77	756.7	218.2
10.79	840.4	303.3	9.79	767.5	221.2
11.77	822.6	296.4	10.79	775.3	225.2
16.04	825.3	297.1	11.77	762.4	227.6
16.79	831.8	302.7	16.04	754.5	223.3
17.69	828.6	300.0	16.79	759.5	223.8
17.92	835.0	301.0	17.69	771.3	225.5
22.00	839.5	300.5	17.92	776.0	225.9
22.71	838.5	302.0	22.00	782.7	223.4
23.88	840.7	302.1	22.71	789.3	225.3
26.83	834.7	298.5	23.88	800.1	226.0
28.04	834.6	297.7	26.83	796.2	220.1
29.73	841.3	302.4	28.04	785.6	219.1
30.83	841.2	301.3	29.73	778.1	219.1
31.88	849.1	302.3	30.83	802.4	223.7
32.96	846.6	303.2	31.88	816.3	226.4
33.71	849.6	303.9	32.96	809.1	228.3
34.83	850.8	303.5	33.71	804.1	226.5
36.04	844.4	300.4	34.83	828.5	229.9
36.77	842.4	300.5	36.04	802.1	226.6
37.67	841.1	301.0	36.77	809.5	227.0
39.96	853.4	303.6	37.67	813.4	228.1
41.00	852.7	300.8	39.96	832.3	231.1
45.85	866.3	305.5	41.00	829.1	225.1
48.00	871.1	305.7	45.85	848.7	232.0
49.88	873.4	307.1	48.00	841.1	230.3
52.98	876.2	310.6	49.88	849.2	236.9
54.58	866.6	304.6	52.98	837.5	237.1
54.88	878.1	309.7	54.58	851.9	239.2
58.79	860.2	309.1	54.88	845.3	236.0
61.96	879.6	312.4	58.79	822.7	233.9
62.96	880.6	313.2	61.96	855.6	238.7
64.83	887.2	316.0	62.96	846.3	239.1
65.75	887.4	315.6	64.83	856.9	241.7
69.83	884.4	314.2	65.75	850.9	241.7
70.75	888.2	315.1	69.83	847.2	241.8
71.85	887.8	313.9	70.75	829.4	235.4
73.73	888.4	314.3	71.85	852.1	240.7
76.67	876.3	312.5	73.73	844.6	239.4
79.92	881.4	317.8	76.67	820.4	234.4
83.00	873.3	316.1	79.92	840.6	242.8
85.81	860.4	318.1	83.00	827.0	240.9
89.71	838.6	313.9	85.81	806.7	242.9
90.67	839.2	312.7	89.71	782.1	239.4
91.71	836.7	312.3	91.71	777.0	235.0
95.67	831.8	306.6	95.67	761.4	229.9
Error	0.49%	0.62%	Error	1.4%	1.2%

Table 1: Flux density measurements. Error bars are not given for each point individually, but rather for each data set as a whole in the form of a constant percentage error calculated from the scatter in each light curve, as described in Section 3. The estimated percentage errors are listed in the last row of the table. These flux density values include a constant offset due to a contribution from the surrounding Einstein ring of radio emission.

Error Estimates as a Function of “True” α and “Assumed” α

“Fitted” α	$\alpha_{true} = 0.5$	$\alpha_{true} = 0.75$	$\alpha_{true} = 1.00$	$\alpha_{true} = 1.25$	$\alpha_{true} = 1.50$
0.5	$1\sigma = 0.42$	$1\sigma = 0.42$	$1\sigma = 0.48$	$1\sigma = 0.59$	$1\sigma = 0.82$
	$2\sigma = 1.72$	$2\sigma = 1.35$	$2\sigma = 1.40$	$2\sigma = 1.46$	$2\sigma = 1.73$
0.75	$1\sigma = 0.48$	$1\sigma = 0.41$	$1\sigma = 0.44$	$1\sigma = 0.56$	$1\sigma = 0.70$
	$2\sigma = 1.80$	$2\sigma = 1.23$	$2\sigma = 1.32$	$2\sigma = 1.40$	$2\sigma = 1.80$
1.00	$1\sigma = 0.60$	$1\sigma = 0.42$	$1\sigma = 0.42$	$1\sigma = 0.54$	$1\sigma = 0.69$
	$2\sigma = 2.04$	$2\sigma = 1.16$	$2\sigma = 1.11$	$2\sigma = 1.23$	$2\sigma = 1.59$
1.25	$1\sigma = 0.67$	$1\sigma = 0.49$	$1\sigma = 0.48$	$1\sigma = 0.49$	$1\sigma = 0.68$
	$2\sigma = 2.29$	$2\sigma = 1.42$	$2\sigma = 1.22$	$2\sigma = 1.30$	$2\sigma = 1.68$
1.50	$1\sigma = 0.98$	$1\sigma = 0.67$	$1\sigma = 0.26$	$1\sigma = 0.55$	$1\sigma = 0.61$
	$2\sigma = 2.82$	$2\sigma = 1.79$	$2\sigma = 1.18$	$2\sigma = 1.49$	$2\sigma = 1.49$

Table 2: Results of Monte Carlo simulations for various “true” and “assumed” structure functions. In each case, the synthetic light curves were created using a structure function with a given α (the “true” α). A structure function was then fit to the synthetic light curves with the condition that α be fixed at a given value (the “assumed” α). This fitted structure function was then used to get the time delay. The time delay derived from this technique was compared to the actual time delay in each case. For each pair of true α and assumed α , 1,000 synthetic light curves were produced. In each case the accuracy of the time delay fitting was expressed as 1σ and 2σ error bars, given in units of days.

Results with Monte Carlo Error Estimates (95% confidence)

ν	T (days)	R	C_o (mJy)
8 GHz	$9.6^{+1.3}_{-1.2}$	$3.2^{+0.3}_{-0.4}$	110^{+80}_{-110}
15 GHz	$11.3^{+2.0}_{-1.8}$	$4.3^{+0.5}_{-0.8}$	180^{+100}_{-140}
averaged	$10.1^{+1.1}_{-1.0}$	$3.4^{+0.2}_{-0.4}$	

Table 3: Results of fitting the time delay (T), variable ratio (R) and excess constant component (C_o) to minimize the PRHQ statistic for the 8 GHz and 15 GHz light curves. The error bars (95% confidence) are determined from Monte Carlo simulations. The last line of the table shows the averaged result from the two light curves.

Results with Jackknife Error Estimates (95% confidence)

ν	T (days)	R	C_o (mJy)
8 GHz	$9.6^{+1.7}_{-2.6}$	$3.2^{+0.2}_{-0.3}$	110^{+70}_{-80}
15 GHz	$11.3^{+4.3}_{-2.0}$	$4.3^{+0.4}_{-0.6}$	180^{+90}_{-150}
averaged	$10.1^{+1.5}_{-1.6}$	$3.4^{+.2}_{-.2}$	

Table 4: Results of fitting the time delay (T), variable ratio (R) and excess constant component (C_o) to minimize the PRHQ statistic for the 8 GHz and 15 GHz light curves. The error bars (95% confidence) are determined from jackknife samples. The last line of the table shows the averaged result from the two light curves.

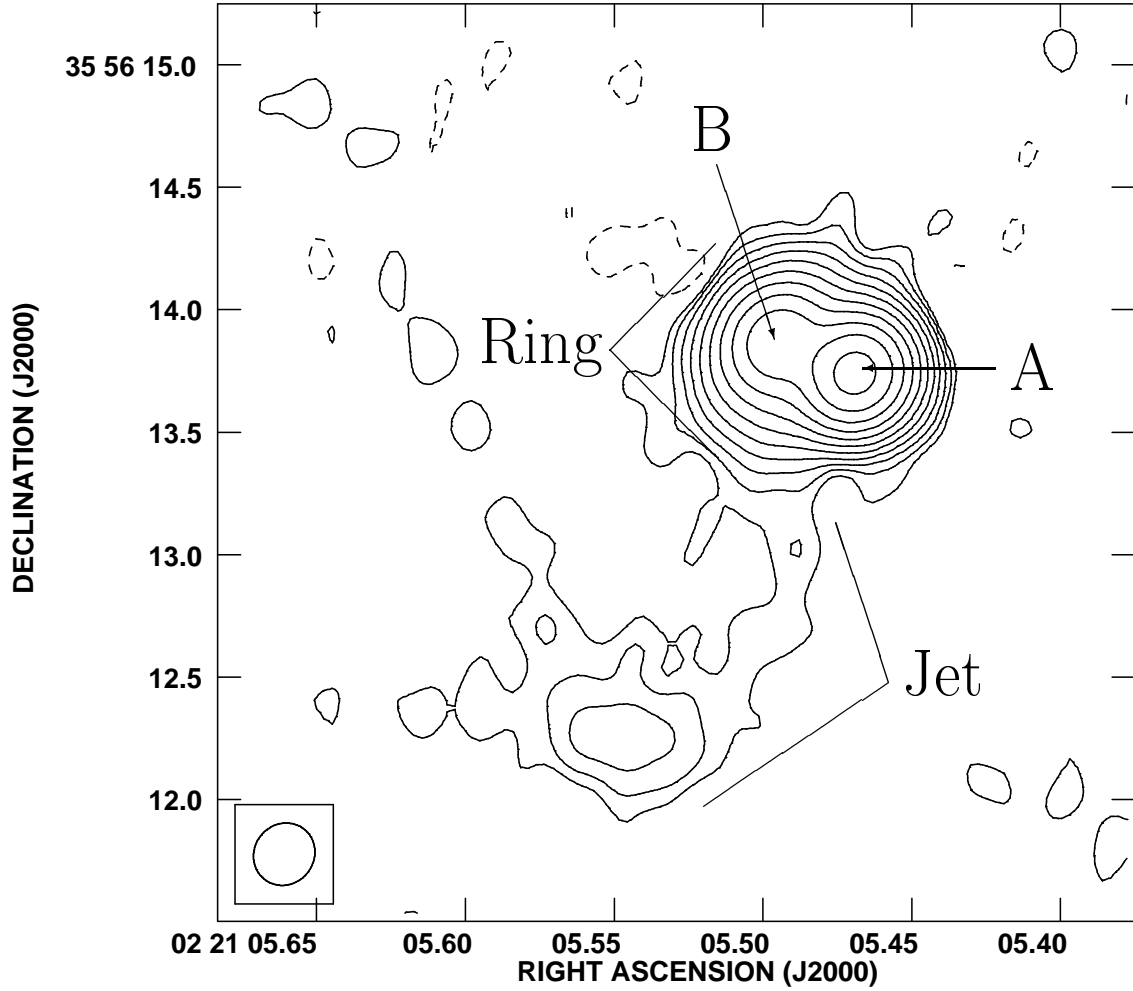


Fig. 1.— VLA 8 GHz map of 0218+357. Contour levels are $(0.6 \text{ mJy/beam}) \times (-4, -2, -1, 1, 2, 4, 8, 16, 32, 64, 128, 256, 512, 1024, 2048)$. The peak brightness is 836 mJy/beam, and the beam major and minor axes are 263 and 250 milliarcseconds at a position angle of 3° .

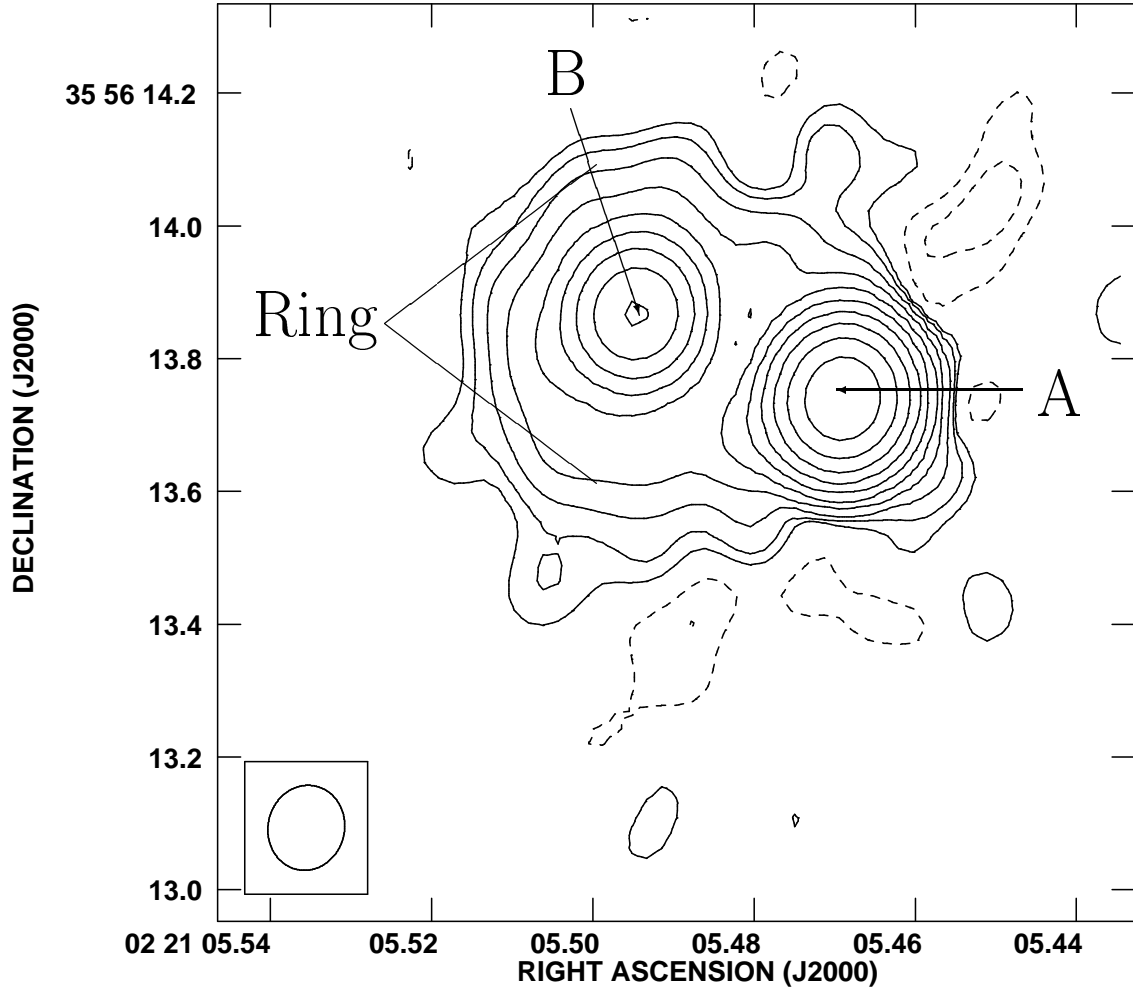


Fig. 2.— VLA 15 GHz map of 0218+357. Contour levels are $(0.8 \text{ mJy/beam}) \times (-4, -2, -1, 1, 2, 4, 8, 16, 32, 64, 128, 256, 512, 1024, 2048)$. The peak brightness is 775 mJy/beam, and the beam major and minor axes are 174 and 131 milliarcseconds at a position angle of 15° .

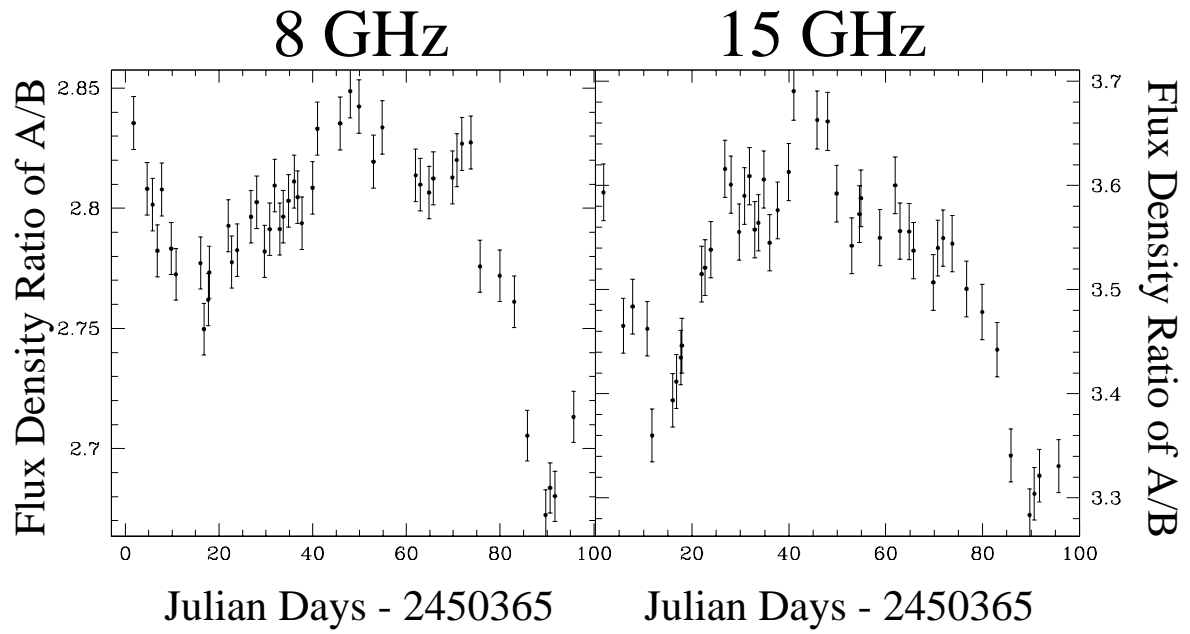


Fig. 3.— Ratios of the A and B flux densities plotted as a function of time.

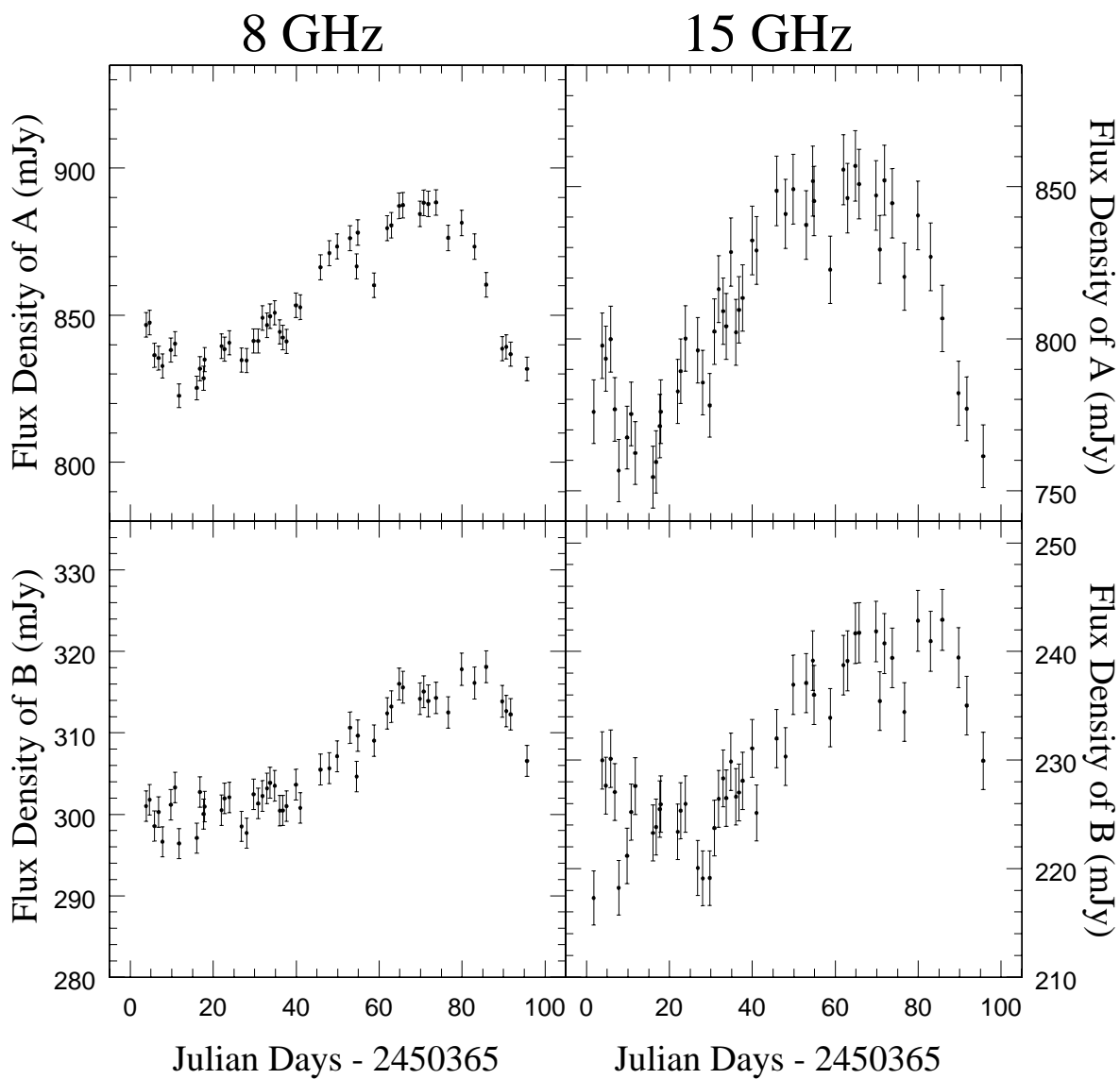


Fig. 4.— Light curves of the compact components of gravitational lens 0218+357. These light curves include a constant offset due to a contribution from the surrounding Einstein ring of radio emission.

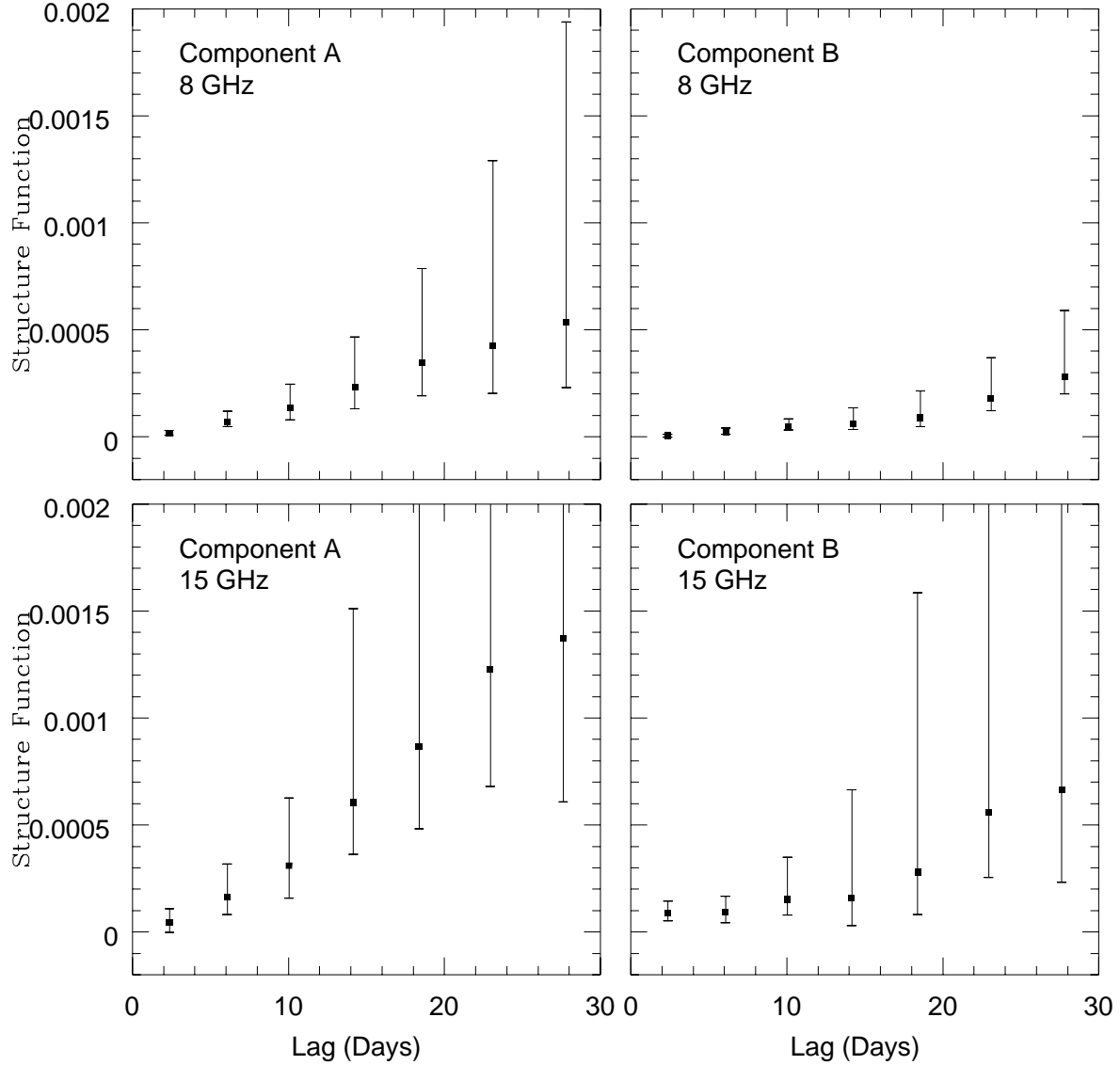


Fig. 5.— Empirical point estimates of the structure function for the 8 GHz and 15 GHz light curves for A and B. The points are binned in groups of 100. The error bars are derived from Monte Carlo simulations and show that the differences in the structure functions are not significant. Structure functions are computed according to equation (1), with flux densities expressed in natural logarithm units referred to 1 mJy.

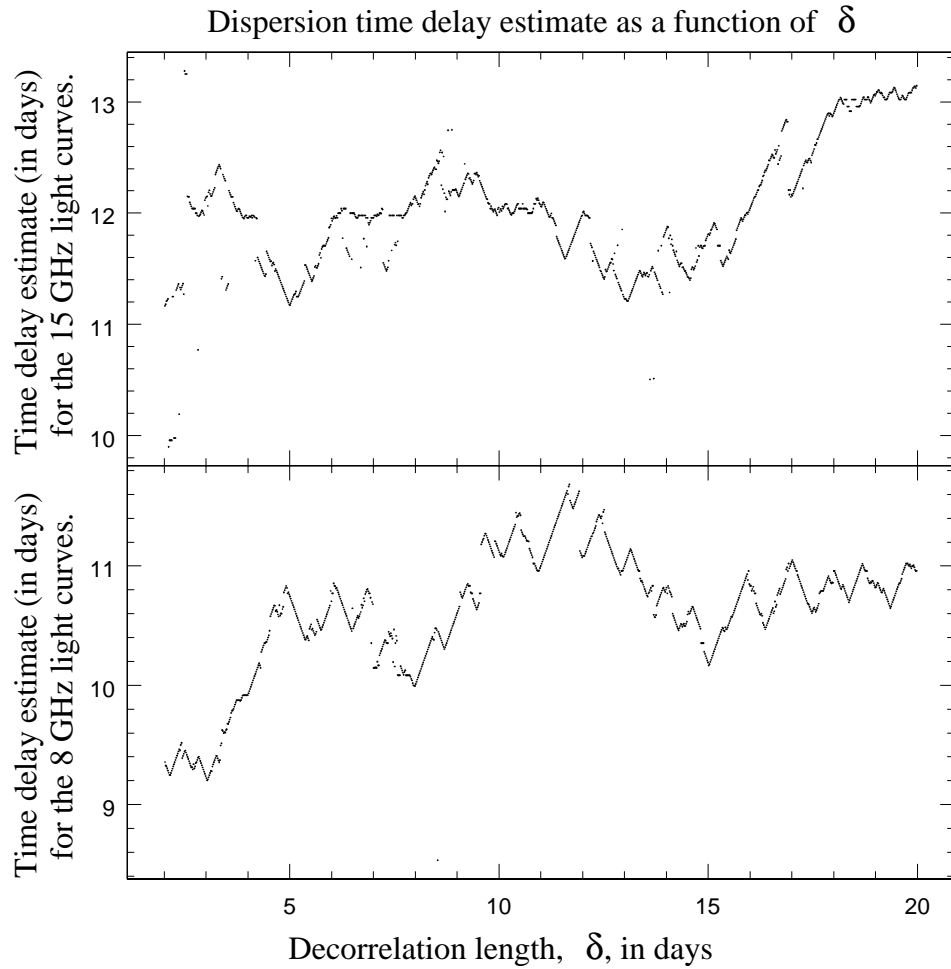


Fig. 6.— The best fit time delay and variable ratio as determined by the minimum dispersion method, plotted as a function of the “decorrelation length”, δ (in days). Since we have no a priori knowledge of δ , this technique does not provide definitive values for the parameters.

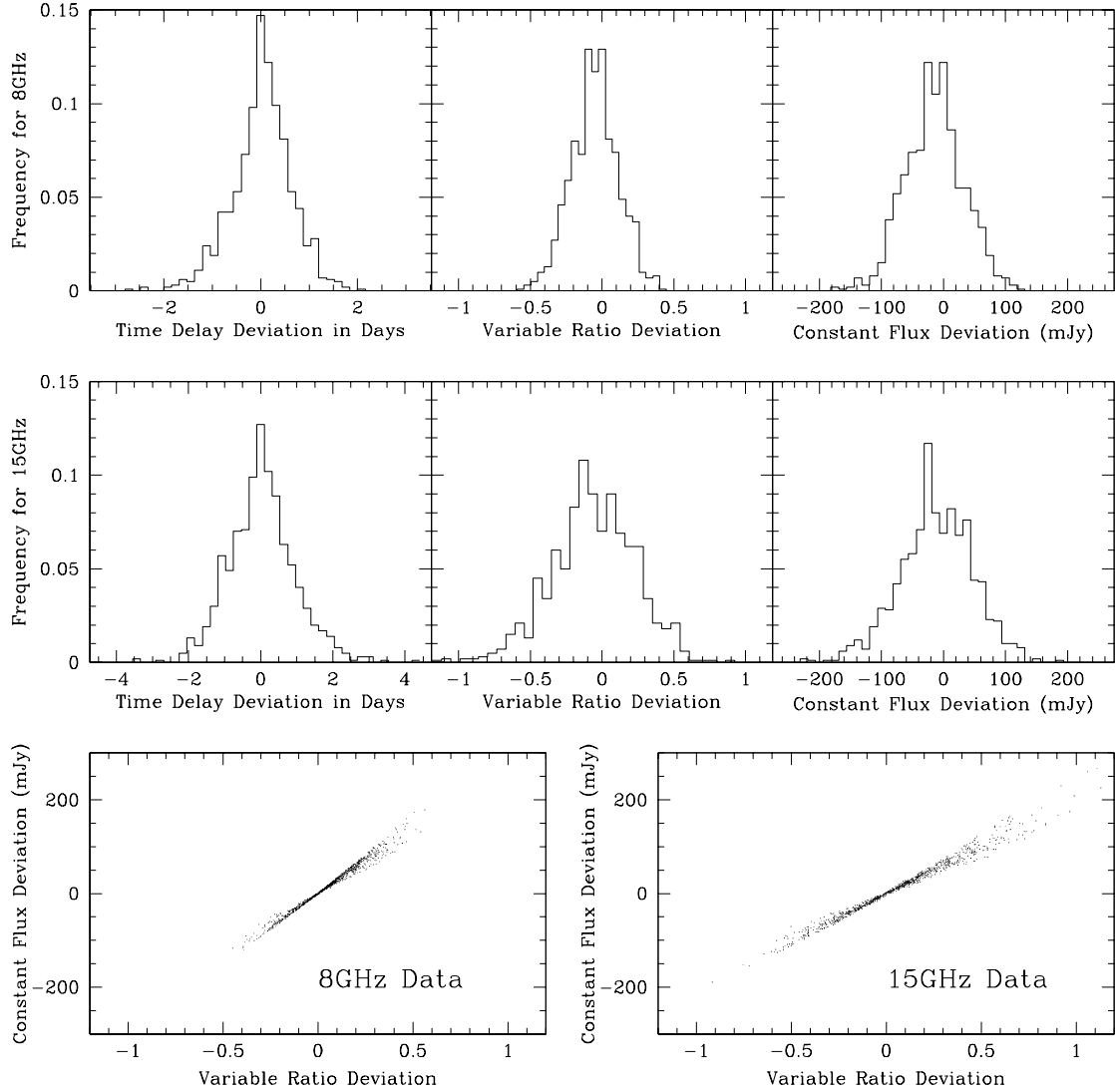


Fig. 7.— Histograms that display the error distribution for each parameter as deduced from Monte Carlo simulations of the 8 GHz and 15 GHz light curves. The “deviation” in each case is the difference between the fitted and true values. The bottom two panels compare the C_o deviation to the R deviation for each simulated data set. There is clearly a high correlation between the two. This demonstrates that if either C_o or R is known *a priori*, the other parameter is well constrained. However, the two parameters cannot be constrained simultaneously with these data.

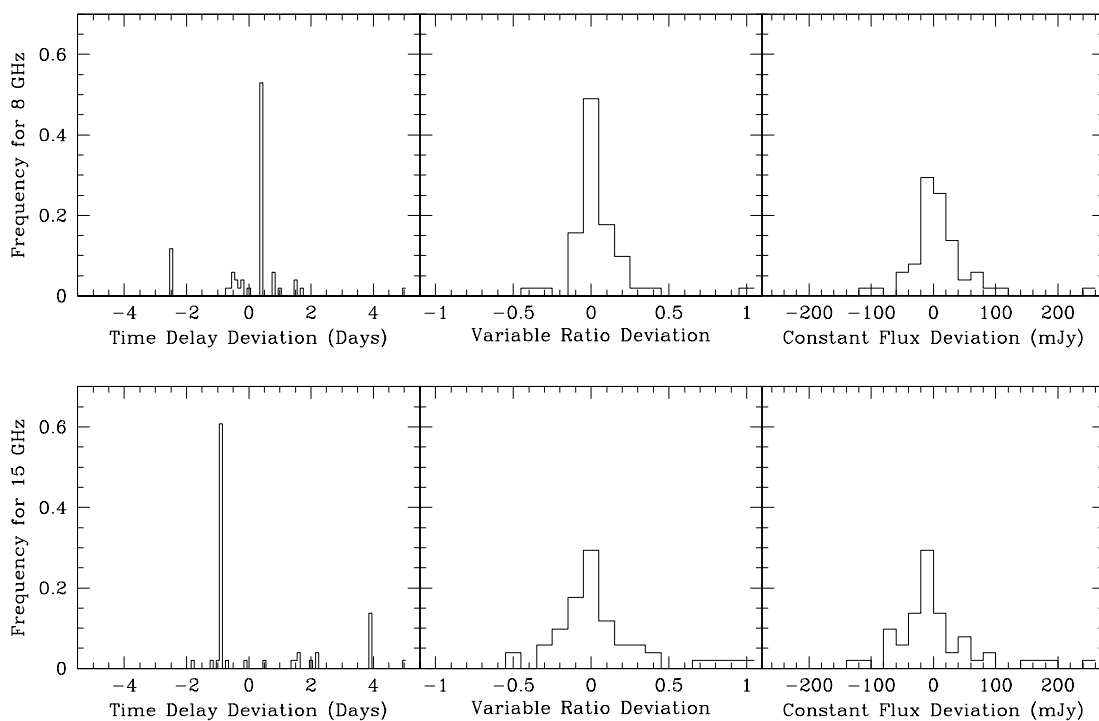


Fig. 8.— Histograms that display the error distribution for each parameter as deduced from jackknife samples of the 8 GHz and 15 GHz light curves. These distributions include a rescaling of the horizontal axes by the “expansion factor” $(N - 1)/N^{1/2}$ (Efron & Tibshirani 1993).

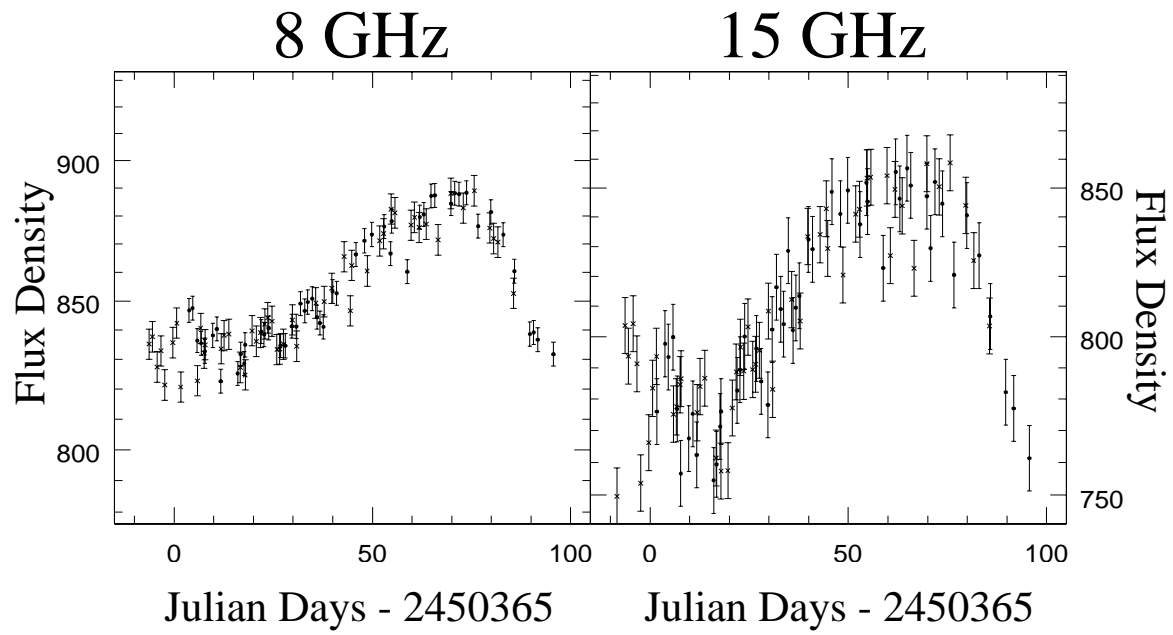


Fig. 9.— Light curves of component A (filled circles) and component B (X's) superimposed according to the best-fit time delays and magnification ratios.